

# Chapter 8

## Hydrologic Assessment of the Uncertainty of Six Remote Sensing Precipitation Estimates Driven by a Distributed Hydrologic Model in the Blue Nile Basin



Hadir Abdelmoneim, Mohamed R. Soliman,  
and Hossam M. Moghazy

**Abstract** Because of the sparseness of the ground monitoring network, precipitation estimations based on satellite products (PESPs) are currently requisite tools for hydrological simulation research and applications. The evaluation of six global high-resolution PESPs (TRMM 3B42V7, GPGP-1DD, TRMM 3B42RT, CMORPH-V1.0, PERSIANN, and PERSIANN-CDR) is the ultimate purpose of this research. Additionally, the distributed Hydrological River Basin Environmental Assessment Model (Hydro-BEAM) is used to investigate their potential effects in streamflow predictions over the Blue Nile basin (BNB) during the period 2001 to 2007. The correctness of the studied PESPs is assessed by applying categorical criteria to appraise their performances in estimating and reproducing precipitation amounts, while statistical indicators are utilized to determine their rain detection capabilities. Our findings reveal that TRMM 3B42V7 outperforms the remaining product in both the estimation of precipitation and the hydrological simulation, as reflected in highest NSE and  $R^2$  values ranges from 0.85 to 0.94. Generally, the TRMM 3B42V7 precipitation product exhibits tremendous potential as a substitute for precipitation estimates in the BNB, which will provide powerful forcing input data for distributed hydrological models. Overall, this study will hopefully provide a better comprehension of the usefulness and uncertainties of various PESPs in streamflow simulations, particularly in this region.

**Keywords** Satellite · Rainfall · Products · Hydro-BEAM · Blue Nile Basin · Hydrological model

---

H. Abdelmoneim (✉) · M. R. Soliman · H. M. Moghazy  
Faculty of Engineering, Alexandria University, Alexandria, Egypt

M. R. Soliman  
Faculty of Engineering, Beirut Arab University, Beirut, Lebanon

## 8.1 Introduction

Precipitation inputs are a vital source for research and applications of hydrologic simulations, specifically in data-scarce areas where the rareness of gauging networks curtails the accessibility of precise and credible rainfall data. However, measured ground gauging data are either sparse in time and space in several areas, or ungauged regions exist in several populous areas of the world, such as developing regions (Behrangi et al. 2011).

Many high-resolution precipitation estimations based on satellite products (PESPs) have been operatively obtainable over a quasi-global scale in recent decades at high temporal (3 h) and spatial (almost 0.25°) resolutions. These products are potential substitutes for rainfall datasets in global hydrometeorological studies and applications. Commonly used satellite precipitation estimates include Tropical Rainfall Measuring Mission (TRMM) data (Huffman et al. 2007), the National Oceanic and Atmospheric Administration (NOAA)'s Climate Prediction Center (CPC) MORPHing technique data (CMORPH) (Joyce et al. 2004), the Global Satellite Mapping of Precipitation (GPM) data (Kubota et al. 2007) and the Precipitation Estimation from Remotely Sensed Imagery using Artificial Neural Networks (PERSIANN) data (Sorooshian et al. 2000). These PESPs are capable of monitoring temporal precipitation variations and spatial patterns at diminutive resolutions. Additionally, they provide useful tools to promote hydrological purposes for fully distributed hydrological models, especially in data-sparse regions and regions with nonexistent data (Sun et al. 2016).

Reviews of recent studies allow the studies to be classified into two categories: the first focuses on evaluating and comparing PESPs against the estimates of local gauging networks (Ali et al. 2017; Habib et al. 2012; Hirpa et al. 2010; Fenta et al. 2018; Gebere et al. 2015; Gebremicael et al. 2017; Jiang et al. 2018; Romilly and Gebremichael 2011). Among these studies, Jiang et al. (2018) used continuous statistical indices (RMSE, CC, and RE) and categorical metrics (POD, FBI, FAR, and ETS) to evaluate the accuracies of two high-resolution PESPs (TRMM 3B42V7 and CMORPH) for the interval 2010 to 2011 in Shanghai. Additionally, Gebremicael et al. (2017) evaluated eight PESPs against in situ rainfall data over the upper Tekeze-Atbara basin, which characterizes by the composite topography of Ethiopia.

The second category involves the evaluation and investigation of the impacts of PESPs through streamflow simulations driving hydrological models over various regions (Alazzy et al. 2017; Bitew and Gebremichael 2011; Bitew et al. 2012; Jiang et al. 2012; Lakew et al. 2017; Sun et al. 2016; Stisen and Sandholt 2010; Tong et al. 2014; Xue et al. 2013; Wang et al. 2015). For instance, Sun et al. (2016) statistically evaluated the four latest PESPs (CMORPH-CRT, CMORPH-CMA, CMORPH-BLD, and TRMM 3B42V7) over the Huaihe River basin in eastern China. Additionally, the authors employed the variable infiltration capacity (VIC) distributed model to predict the river flow rate within the period 2003–2012. The results revealed that CMORPH-CMA had a perfect capability for improving the distribution of precipitation and hydrological applications. They also recommend this CMORPH-CMA as an alternative rainfall input source for this region.

Li et al. (2019) assessed three PESP (TMPA 3B42V7, PERSIANN-CDR, and GPM IMERG) at daily and monthly timesteps in the lower Mekong River basin, which is located in Southeast Asia. They also investigated the potential of these PESP to predict streamflows driven by a distributed geomorphology-based hydrological model (GBHM). Their findings revealed that the IMERG product can be used to reproduce precipitation well and accurately, particularly in the detection of heavy rainfall events. The hydrological simulations forced by the three datasets revealed acceptable precisions at major stations. Moreover, simulated results forced by IMERG outperformed the remaining products, as the smallest RRMSE values and largest NSE values were calculated for the IMERG product.

The Blue Nile River is a vital tributary of the Nile River and provides the greatest portion to the flow of the Nile River, approximately 60%. The area of the Blue Nile River suffers from a sparse rain gauge network with an uneven distribution. In addition, the region is characterized by complex topography, a variable climate, and a large geographical area. Hence, the use of PESP as driving forces for hydrological models is necessary after the determination of the accurate product for this basin. A few prior studies focused on the evaluation of PESP over small basins in the Ethiopian highland, such as the studies by Bitew and Gebremichael (2011) and Bitew et al. (2012). Additionally, Gebremichael et al. (2017) explored the relationships between PESP and topography to understand the conceivable miscalculations generated by the rugged land in the area. To the best of our knowledge, no study has evaluated PESP and investigated their ability to predict streamflow over the entire BNB. Therefore, the present research focuses on the comprehensive hydrologic assessment of the uncertainty of six PESP (TRMM 3B42V7, TRMM 3B42RT, PERSIANN, PERSIANN-CDR, CMORPH-V1.0, and GPGP-1DD) in the Blue Nile Basin (BNB). This work aims to compare and evaluate the performance of six high-resolution PESP in capturing the magnitude of rainfall over the BNB against data from land gauges within the period 2001 to 2007. Additionally, the effects of the studied PESP on hydrologic simulation procedures at the target basin is investigated, driven by the distributed Hydrological River Basin Environmental Assessment Model (Hydro-BEAM), which was established by Kojiri et al. (1998). This attempt is valuable as it relates to the use of high-resolution PESP for monitoring and predicting streamflows in the BNB and in similar watersheds that are characterized by common climate and topography.

## 8.2 Materials and Methods

### 8.2.1 Study Area

The Nile River is a transboundary river, and its tributaries travel through eleven countries. The Nile River has two vital tributaries: the White Nile River and the Blue Nile River. The Blue Nile River, chosen in this paper as the study area, is a

crucial Nile River tributary originating from the Ethiopian Plateau, flowing into Sudan, and meeting the White Nile River at Khartoum to form the main Nile River. This river is considered the Nile River's critical tributary, as it provides a large portion of the flow of the Nile River, approximately 60%. The BNB is located between latitudes 16°2'N and 7°40'N and longitudes 32°30'E and 39°49'E in the Ethiopian Highlands, as shown in Fig. 8.1. The river originates from the outlet of Lake Tana, flowing south in the Ethiopian highlands and then northwest; its length is approximately 900 km from Lake Tana to the Sudanese border, and the river ends when it reaches the White Nile River in Khartoum, Sudan (Samy et al. 2015). The drainage area of the BNB is estimated at approximately 325,000 km<sup>2</sup> (Ragab and Valeriano 2014). The catchment includes a range of topographic conditions, sizes, climatic conditions, slopes, geological features, drainage patterns, vegetation covers, soils, and anthropogenic activity.

The topography of the watershed is split into two distinct features: the first comprises flat topography in the lowlands of Sudan, and the second includes mountainous topography in the Ethiopian Plateau, where the regions containing high, steep mountains, when combined, overlay approximately 65% of the drainage area (Gebrehiwot et al. 2011). The Ethiopian Plateau is situated at altitudes of 2,000–3,000 m, with certain areas reaching heights up to or above 4,000 m, as

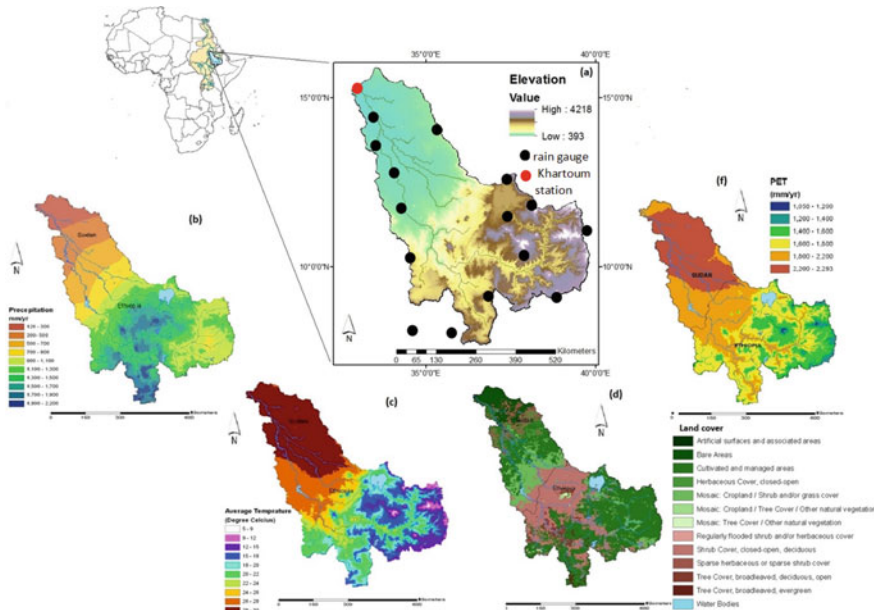


**Fig. 8.1** a The BNB's location in the Ethiopian Highlands and (right) a DEM map of the BNB; b the average annual precipitation distribution over the BNB; c the average annual temperature distribution over the BNB; d soil types in the BNB; and f the average annual evapotranspiration distribution over the BNB (Abd-El Moneim et al. 2019)

illustrated in Fig. 8.1a (Ragab and Valeriano 2014). Precipitation over the BNB varies remarkably with altitude from nearly below 200 mm/yr in the northeastern part of the basin to 2,000 mm/yr in Ethiopia's highlands, as displayed in Fig. 8.1b (Awulachew et al. 2008). In the northeastern clay plains of Sudan, the greatest mean annual temperatures occur. In Sudan, 24 and 44 °C are the daily minimum and maximum temperatures in May, and 14 and 33 °C are the daily minimum and maximum temperatures in January, respectively. The Ethiopian Plateau region is characterized by lower monthly mean minimum temperatures, ranging from 3 to 21 °C, between December and February, as shown in Fig. 8.1c (Awulachew et al. 2008). The spatial distribution of evapotranspiration in the region is similar to those of rainfall and temperature, with considerable variations across the basin and a notable correlation with altitude, as illustrated in Fig. 8.1f (Awulachew et al. 2008).

## ***8.2.2 In Situ Precipitation and Discharge Datasets***

Measured datasets play pivotal roles in the quantitative evaluation of PESPs. Due to the scarcity of data in developing regions, rainfall and Blue Nile flow rate data are collected through a process that requires the study time interval to be set from 2001 to 2007, according to the availability of measured datasets. Additionally, these data were collected on a monthly timestep from published reports by the Ministry of Water Resources and Irrigation (MWRI) in Egypt (MWRI 1998a; b). Monthly rainfall data from 15 ground rain gauges and the monthly discharge data from the Khartoum station are used in the current study, as shown in Fig. 8.1a. Incorrect values, such as negative and missed values, were rejected, which may make the comparison unreliable.

## ***8.2.3 Remote Sensing Precipitation Estimation Products***

### **8.2.3.1 TRMM Products**

The National Space Development Agency (NSDA) and the National Aeronautics and Space Administration (NASA) jointly established the TRMM on 27 November 1997. This satellite is primarily intended for weather and climate science monitoring and for observations of tropical precipitation. The main pieces of rainfall equipment on this satellite are the Visible and Infrared Radiometer Network (VIRS), the TRMM Microwave Imager (TMI), and the Precipitation Radar (PR) (Kummerow et al. 1998). The TRMM Multisatellite Precipitation Analysis (TMPA) rainfall products were blended with other high-quality rainfall estimate algorithms, such as infrared-based (IR) and merged active/passive microwave (PMW) rainfall estimations, and these merged data were added to other numerous source dataset rainfall product blends, according to Huffman et al. (2007). The three

following steps are carried out for this product: first, the PMW rainfall estimates are calibrated and combined to produce the utmost reliable PMW estimates; next, the calibrated PMW estimates are utilized to produce IR rainfall estimations; and finally, the PMW and IR rainfall estimations are combined to provide the best TMPA rain estimations (Alazzy et al. 2017). Two versions of TMPA products are accessible with coverage between the longitudinal range 180°W–180°E and the latitudinal range 50°S–50°N as well as a fine spatial resolution ( $0.25^\circ \times 0.25^\circ$ ) and a high temporal resolution (3 h): a post-real-time research version (3B42) and a real-time version (3B42RT). The TRMM 3B42V7 product was adjusted via the monthly deviation of the precipitation dataset from the Global Precipitation Climate Center (GPCC) calibration meteorological stations compared to the TRMM 3B42RT product. Furthermore, this product has many computational enhancements and good data precision (Huang et al. 2014). The principal distinction between the two versions is that the post-real-time research product uses monthly ground rainfall data for bias correction. In this study, the TRMM 3B42V7 and 3B42RT datasets used were obtained from <https://giovanni.sci.gsfc.nasa.gov/giovanni/>.

### 8.2.3.2 CMORPH Product

The CMORPH tool of NOAA is a process of rainfall estimation based primarily on passive microwave (PWM) satellite measurements collected from low Earth orbiting (LEO) satellite radiometers; it incorporates a tracking technique using data from infrared (IR) measurements solely to derive a field of cloud motion that is thereafter used to propagate pixels of rainfall (Joyce et al. 2004). The latest satellite rainfall datasets, named the CMORPH-Version 1.0 products, have recently been developed by NOAA-CPC in three product forms: a pure satellite rainfall product (CMORPH-RAW), a gauge-satellite blended product (CMORPH-BLD) and a bias-corrected product (CMORPH-CRT). The CMORPH-RAW is an outcome of satellite-only rainfall estimates created by merging passive microwave-based rainfall estimates the infrared data of various geostationary satellites as well as numerous low orbit satellites. The following can be summarized as the key discrepancies between the ancient version, 0.x, and the new version, 1.0: fixed versions of satellite rainfall datasets and a fixed algorithm were used during the whole TRMM/GPM period (1998–present) in the latest version, 1.0, particularly to ensure the best possible homogeneity, whereas the ancient version, 0.x, has been developed since 2002 using various enhanced algorithms and developing satellite-based inputs of rainfall product versions (Joyce et al. 2010). In this work, the CMORPH-V1.0 RAW datasets were used; these datasets are freely available at <ftp://ftp.cpc.ncep.noaa.gov/precip/CMORPHV1.0/>.

### 8.2.3.3 PERSIANN Products

The PERSIANN product (Hsu et al. 1997) is one of the accepted estimates of global precipitation used to estimate historical precipitation from March 2000 until now. For its global precipitation estimations, the product uses the neural network method to derive relationships between IR and PMW estimates from Geostationary Earth Orbiting (GEO) and LEO satellite imagery, respectively (Sorooshian et al. 2000). First, the Grid Satellite (GridSat-B1) IR record archive (Knapp 2008) was used in the latest version of the PERSIANN-Climate Data Record (PERSIANN-CDR) product as an input to the eligible PERSIANN model; then, the Global Precipitation Climatology Project (GPCP) version 2.2 updated the biases in the predicted PERSIANN precipitation values on a monthly time scale (Ashouri et al. 2015). The parameters of the PERSIANN model were pretrained using stage-IV hourly precipitation data from the National Centers for Environmental Prediction (NCEP); later, the model was run using the full GridSat-B1 IR historical record with fixed model parameters as indicated in the calibration scheme by Ashouri et al. (2015). This product is available with a daily temporal resolution and a fine spatial resolution ( $0.25^\circ \times 0.25^\circ$ ). Precipitation datasets are available from 1 January 1983 to the present. In the current research, the two PERSIANN product (PERSIANN and PERSIANN-CDR) datasets that were used were freely obtained from <http://chrsdata.eng.uci.edu/>.

### 8.2.3.4 GPCP-1DD Product

The Global Precipitation Climatology Project One Degree Daily (GPCP-1DD) product incorporates IR and PMW precipitation estimates with the GPCC gauging dataset (Huffman et al. 1997). In the GPCP-1DD product, the PMW precipitation estimates depend on the Special Sensor Microwave/Imager (SSM/I) data from the Defense Meteorological Satellite Program (DMSP, US), while the IR data are principally obtained from the precipitation index (PI) data of the Geostationary Operational Satellite (GOES) (Xie and Arkin 1995). This product has the advantage of integrating precipitation estimate information by incorporating the strengths of different data types from multiple data sources. The GPCP-1DD product provides daily data on global precipitation grid with a resolution of  $1^\circ \times 1^\circ$ . The GPCP-1DD datasets are available to download from <https://ftp://ftp.cgd.ucar.edu/archive/PRECIP/>.

Overall, Table 8.1 presents the six PESP (TRMM 3B42V7, GPGP-1DD, TRMM 3B42RT, CMORPH-V1.0, PERSIANN, and PERSIANN-CDR) used in this work.

**Table 8.1** Summaries of the six PESPes evaluated in this work

Datasets	CMORPH-V1.0	TRMM 3B42v7	TRMM 3B42RT	PERSIANN	PERSIANN-CDR	GPCP-IDD
Spatial coverage	180°W–180°E, 50°N–50°S Quasi-global	180°W–180°E, 50°N–50°S Quasi-global	180°W–180°E, 50°N–50°S Quasi-global	180°W–180°E, 60°N–60°S Quasi-global	180°W–180°E, 60°N–60°S Quasi-global	180°W–180°E, 50°N–50°S Quasi-global
Temporal coverage	1998–present	1998–April 2014	March 2000–present	March 2000–present	1983–January 2017	1997–July 2011
Datasets source	TMI, AMSR-E, SSM/I, SSMIS, AMSU, MHS, IR vectors	TCl, TMI, SSMI, SSMIS, AMSR-E, AMSU, MHS, MW-VAR, (IR), gauge	HQ, Mw-VAR (IR)	(TMI, AMSR-E, SSM/I, SSMIS, AMSU, MHS)-cal. IR	GRIDSAT-IRWIN, GPCP monthly precipitation	SSM/I- and SSMIS-TMPI (IR), TOVAS, AIRS, GPCP monthly
Spatial resolution	$0.25^\circ \times 0.25^\circ$	$0.25^\circ \times 0.25^\circ$	$0.25^\circ \times 0.25^\circ$	$0.25^\circ \times 0.25^\circ$	$0.25^\circ \times 0.25^\circ$	$1^\circ \times 1^\circ$
Temporal resolution	Daily	Daily	Daily	Daily	Daily	Daily
Data download Web site	<a href="ftp://ftp.cpc.ncep.noaa.gov/precip/CMORPH_V1.0/RAW/">ftp://ftp.cpc.ncep.noaa.gov/precip/CMORPH_V1.0/RAW/</a>	<a href="ftp://ftp.cgd.ucar.edu/archive/PRECIP/TRMM/">ftp://ftp.cgd.ucar.edu/archive/PRECIP/TRMM/</a>	<a href="https://giovanni.gsfc.nasa.gov/giovanni/">https://giovanni.gsfc.nasa.gov/giovanni/</a>	<a href="http://chrsdata.eng.uci.edu">http://chrsdata.eng.uci.edu</a>	<a href="http://chrsdata.eng.uci.edu">http://chrsdata.eng.uci.edu</a>	<a href="ftp://meso.gsfc.nasa.gov/pub/idd-v1.2/">ftp://meso.gsfc.nasa.gov/pub/idd-v1.2/</a>



### 8.2.4 Hydro-BEAM Model

Hydro-BEAM is a physically based distributed hydrological model established by Kojiri et al. (1998). The model was confined to environments characterized by moist circumstances until the model was adjusted for simulations of flash flood events in arid wadis (Abdel-Fattah et al. 2015; Saber et al. 2013) and semiarid basins (Abdel-Fattah 2017; Saber and Yilmaz 2016). The model has also been successfully used in numerous hydrological studies under different climatic conditions (e.g., Abd-El Moneim et al. 2017; Saber and Yilmaz 2018; Abdelmoneim et al. 2020). In this study, Hydro-BEAM is used to evaluate the simulated streamflow rates over the BNB based on six PESPs.

The ultimate benefit of the Hydro-BEAM model is the reflection of the spatial variability in catchment features and hydrological processes, where it can reflect hydrological surface and subsurface procedures, such as surface runoff, evapo-transpiration, channel flow routing, groundwater flow, and the intake/release of water on spatially distributed meshed cells. To understand differences in infiltration due to changes in land cover, the model identifies three types of land cover (Sapkta et al. 2010). The model consists of four layers, from A to D, which represent the upper layer for the surface and the remaining layers for the subsurface, as shown in Fig. 8.2a.

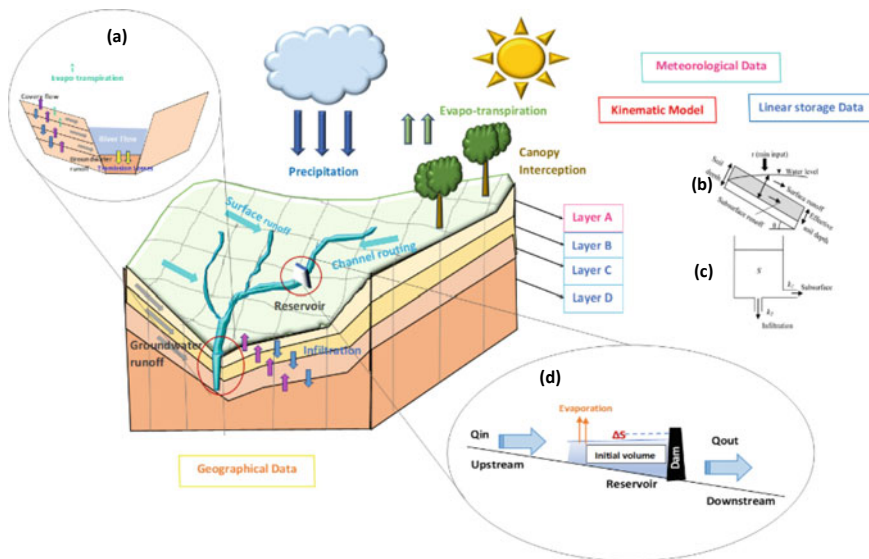


**Fig. 8.2** Conceptual representation of Hydro-BEAM: **a** the basic structure of Hydro-BEAM; **b** the kinematic wave model of the surface layer; **c** the subsurface storage tank layer representation; and **d** the reservoir modeling approach (Kojiri et al. 1998; Abdelmoneim et al. 2020)

Each mesh cell includes details such as surface runoff, land use, slope direction, and a channel's absence/presence (Saber 2010). Layer A represents the surface layer, while layers B to D represent the subsurface layers, as denoted in Fig. 8.2b. In this study, Layer D is neglected as it contains deep groundwater, which has a minor effect on the BNB flow rate. The subsurface layer structures (layers B and C) are based on the linear storage model (see Fig. 8.2c). When the water content storage in these layers reaches a saturated state, the water is discharged into the river combined by layer A. The suggested method can be outlined by the following key processes: (1) watershed modeling is carried out using the methodology of the geographical information system (GIS), (2) the kinematic wave approach is used to calculate the stream routing and surface runoff modeling, (3) transmission loss modeling is calculated using the Walter equation (Walters 1990), and (4) canopy interception losses and (5) the linear storage model are applied for the modeling of groundwater. The spatial resolution implemented in the current research for the BNB is 5 km ( $\sim 0.05^\circ$ ), as indicated in (Abd-El Moneim et al. 2017).

The Blaney-Criddle method was used to determine potential evapotranspiration ( $ET_0$ ) in the model as follows (Karamouz et al. 2013):

$$ET_0 = p (0.46T_{\text{mean}} + 8.13) \quad (8.1)$$

where  $ET_0$  is the potential evapotranspiration (mm/d),  $T_{\text{mean}}$  is the average temperature ( $^\circ\text{C}$ ), and  $p$  is the daily average proportion of daytime hours per year. We can determine the value of  $p$  depending on the estimated latitude of the study area (the number of degrees north or south of the equator) (Karamouz et al. 2013). In this study, daily temperature and daily radiation datasets were retrieved from the Climate Forecast System Reanalysis (CFSR). The datasets are available to download from <https://globalweather.tamu.edu/#pubs>.

Stream routing and surface runoff were calculated using integrated kinematic wave runoff approximations assuming a triangular river cross-section, as shown in Eqs. (8.2, 8.3, 8.4, 8.5):

$$\frac{\partial h}{\partial t} + \frac{\partial q}{\partial x} = fr \quad (8.2)$$

$$q = \alpha(h - d)^{5/3} + ah(h > d) \quad (8.3)$$

$$q = ah \quad (8.4)$$

When  $\begin{pmatrix} h \geq d \\ h \leq d \end{pmatrix}$ ,  $d = \lambda D$

$$\alpha = \frac{\sqrt{\sin \theta}}{n}, \quad a = Ks \frac{\sin \theta}{\gamma} \quad (8.5)$$

where  $q$  is the unit discharge ( $\text{m}^3/\text{s}/\text{m}$ ),  $h$  is the depth of the water (m),  $r$  is the effective precipitation intensity input (m/s) corresponding to the total rainfall infiltration into the soil after evapotranspiration losses are extracted,  $f$  is the ratio of direct runoff, which is equal to the upper soil saturation ratio, layer A (0–1),  $\lambda$  is the porosity,  $\alpha$  and  $m$  are friction constants,  $x$  is the gap to the edge upstream,  $d$  is the saturation pondage (m), and  $D$  is the thickness of the layer (m).

A multilayer linear storage feature model is implemented on the Hydro-BEAM layers B and C to realistically calculate the base flow procedure. The linear storage function model's continuity equation and its dynamic equation are as follows:

$$\frac{dS}{dt} = I - O \quad (8.6)$$

$$O = kS \quad (8.7)$$

where  $I$  is the inflow (m/s),  $S$  is the storage of water (m),  $k$  is the coefficient of runoff (l/s), and  $O$  is the outflow (m/s).

#### 8.2.4.1 Parameters and Calibration

It is noteworthy that the calibration of the model consists of a method that adjusts the parameters to achieve the optimum possible simulation of the realistic runoff measured for some forced data (Jiang et al. 2012). The parameters of the model may display several variations when utilized to simulate the flow rates (Stisen and Sandholt 2010). In the current analysis, the model with individual PESP as inputs was calibrated with the observed streamflow data in the BNB.

The distributed hydrological model for the BNB was calibrated and validated against the available measured streamflow data from 2001 to 2007. The entire study period was classified into two periods: the calibration period, from 2001 to 2003, and the validation period, from 2004 to 2007. Table 8.2 illustrates the respective ranges of the model parameters used, which are dependent on variables such as land use and soil. The calibration regime returns the best parameter values that maximize the Nash–Sutcliffe efficiency (NSE) between the observed and simulated monthly flow rates (Bitew et al. 2012). Such parameters authorize us to parse the influence of the precipitation data source on the model calibration and validation.

### 8.2.5 Statistical Metrics for the Performance Evaluation

Several commonly utilized statistical indicators were employed to qualitatively analyze the overall performance of the six studied PESP versus the gauge-based precipitation measurements. In the current analysis, three different statistical criteria

**Table 8.2** Calibration parameters of the hydrological model for various PESP

Parameters	Symbol	Value range	Units
Horizontal coefficient of permeability	B-layer	0.2	
	C-layer	0.025	
Vertical coefficient of permeability	B-layer	0.4	
Layer thickness	A-layer	0.4	m
Equivalent roughness coefficient	Grass	0.3	$\text{m}^{-1/3}$ s
	Forest	0.7	
	Urban	0.03	
Direct runoff constant	Grass	0.5–0.75	
	Forest	0.3–0.5	
	Urban	0.9	
Porosity	B-layer	15.0	%
	C-layer	15.0	
Finite difference interval	Spatial finite difference interval	2,500	m

were implemented to determine the correctness of the six PESP, as explained in detail below.

### 8.2.5.1 Continuous Statistical Metrics

Continuous verification metrics were used, including the Pearson correlation coefficient (CC), relative error (RE), and root-mean-square error (RMSE). The CC refers to the rainfall variation synchronicity between the in situ rainfall data and PESP, the RE describes the extent of the simulated error compared with that in the rain gauges, and the RMSE was employed to assess the averaged error magnitude. These metrics are calculated as follows:

$$CC = \frac{\sum_{i=1}^n (G_i - G'_i)(P_i - P'_i)}{\sqrt{\sum_{i=1}^n (G_i - G'_i)^2 \sum_{i=1}^n (P_i - P'_i)^2}} \quad (8.8)$$

$$RE = \frac{\sum_{i=1}^n (P_i - G_i)}{\sum_{i=1}^n G_i} \times 100\% \quad (8.9)$$

$$RMSE = \sqrt{\frac{\sum_{i=1}^n (P_i - G_i)^2}{n}} \quad (8.10)$$

where  $P_i$  and  $G_i$  are the  $i$ th pair of PESP and the gauge-based rainfall data,  $n$  reflects the cumulative number of timescales, and  $P'_i$  and  $G'_i$  are the corresponding

average values of the PESP data and the gauge-based data, respectively. The locally measured data and PESP data are considered compatible, without PESP-associated uncertainty, if the RMSE value and RE value are equal to zero and the CC value is equal to 1; this corresponds to higher CCs and lower RMSEs representing higher accuracy of PESP data.

### 8.2.5.2 Categorical Statistical Metrics

To test the detection capability analysis of PESP data against locally measured data at various precipitation thresholds, four categorical statistics were utilized based on the  $2 \times 2$  contingency table. The following indices were used: the detection probability (POD), the frequency bias index (FBI), the false alarm rate (FAR), and the equitable threat score (ETS). POD, also called the hit rate. These indices were used to calculate the occurrences of rainfall by satellites and determine whether rainfall occurrences were detected correctly. FAR denotes that occurrences of rainfall were detected incorrectly. Furthermore, ETS indicates how well PESP data conformed to the measurements of the rain gauges. These indices were calculated as follows:

$$\text{POD} = \frac{H}{H + M} \quad (8.11)$$

$$\text{FAR} = \frac{F}{H + F} \quad (8.12)$$

$$\text{ETS} = \frac{H - \text{hits}}{H + M + F - \text{hits}} \quad (8.13)$$

$$\text{hits} = \frac{(H + M)(H + F)}{H + M + F + Z}$$

$$\text{FBI} = \frac{H + F}{H + M} \quad (8.14)$$

where  $H$  is the correct detection of the measured precipitation number (hits),  $F$  is the precipitation number detected but not measured, and  $M$  is the precipitation number measured but not detected (misses). The ideal POD, FBI, FAR, and ETS values are 1, 1, 0, and 1, respectively. More information and explanations are described in Schaefer (1990), Wilks (2006) and Sun et al. (2016).

### 8.2.5.3 Statistical Evaluation of the Hydrological Model

In both the observed streamflows and the resultant streamflow simulations, statistical evaluation indices were applied to assess the uncertainty and the performance

of six PESPs. The criteria for model performance were tested using three widely utilized statistical indicators for simulations of hydrological models. First, NSE was used to match simulated flows with their statistical goodness values. NSE varies from  $-\infty$  to 1, with greater values signifying stronger correspondences (Legates and McCabe 1999). If  $NSE \leq 0$ , then the model lacks skill concerning the observed mean as a predictor (Lakew et al. 2017). Additionally, the percent bias (Bias) and the determination coefficient ( $R^2$ ) were utilized to assess the agreement between the simulated and measured discharges. These statistical indices were calculated using Eqs. (8.15), (8.16), and (8.17), respectively, as follows:

$$NSE = 1 - \frac{\sum_{i=1}^n (Q_{obs} - Q_{sim})^2}{\sum_{i=1}^n (Q_{obs} - Q'_{obs})^2} \quad (8.15)$$

$$R^2 = \frac{\sum_{i=1}^n (Q_{obs} - Q'_{obs})(Q_{sim} - Q'_{sim})^2}{\sum_{i=1}^n (Q_{obs} - Q'_{obs})^2 \sum_{i=1}^n (Q_{sim} - Q'_{sim})^2} \quad (8.16)$$

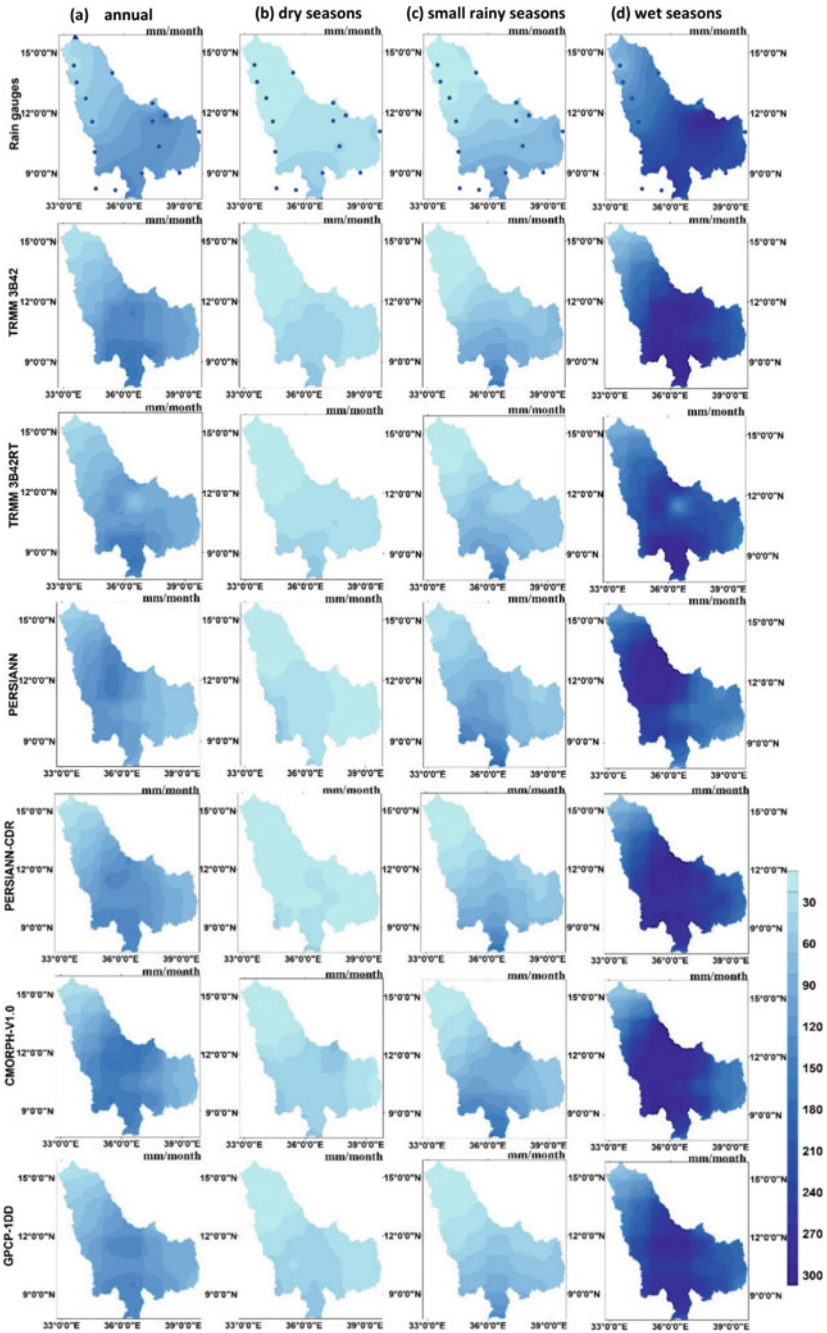
$$Bias = \frac{\sum_{i=1}^n (Q_{sim} - Q_{obs})}{\sum_{i=1}^n Q_{obs}} \times 100\% \quad (8.17)$$

where  $Q_{sim}$  and  $Q'_{sim}$  are the simulated streamflow and the average simulated streamflow, respectively, and  $Q_{obs}$  and  $Q'_{obs}$  are the measured streamflow and the average measured streamflow, respectively. When the values of  $NSE = 1$ ,  $R^2 = 1$ , and  $Bias = 0\%$ , the optimum result occurs.

## 8.3 Results and Discussions

### 8.3.1 Comparison and Assessment of PESPs

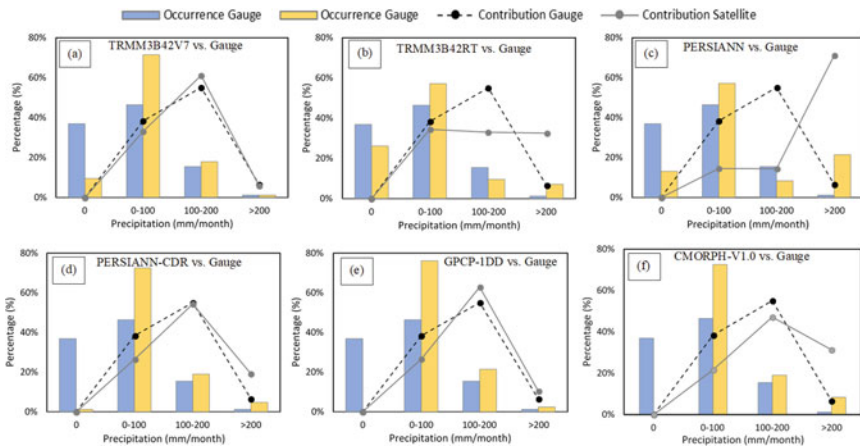
The PESP precision against the in situ rain data was first tested over the BNB to understand the adverse effects of these products on hydrologic models and their correlated uncertainties. The comparative analysis was carried out using statistical approaches to explore and distinguish precipitation patterns and quantify errors over the BNB for six PESPs. The BNB climate is typified by a dry winter season, little spring rain, and a wet summer season (Awulachew et al. 2008). In the summer months between June and September, approximately 70% of the annual precipitation falls (Awulachew et al. 2008). In this study, one year is split into three periods: the dry season (known in Ethiopia as the Bega) (October–February), the period of little rainfall (known in Ethiopia as the Belg) (March–May), and the wet season (known in Ethiopia as the Kiremt). Figure 8.3 displays the spatial distribution maps of the annual average rainfall (column (a)), the dry season (column (b)), the season of little rain (column (c)), and the wet season (column (d)) obtained from



**Fig. 8.3** Distribution maps of annual average (column (a)), dry season (column (b)), small rainy season (column (c)) and rainy season (column (d)) rainfall amounts obtained from PESP over the BNB during 2001–2007 (mm/month)

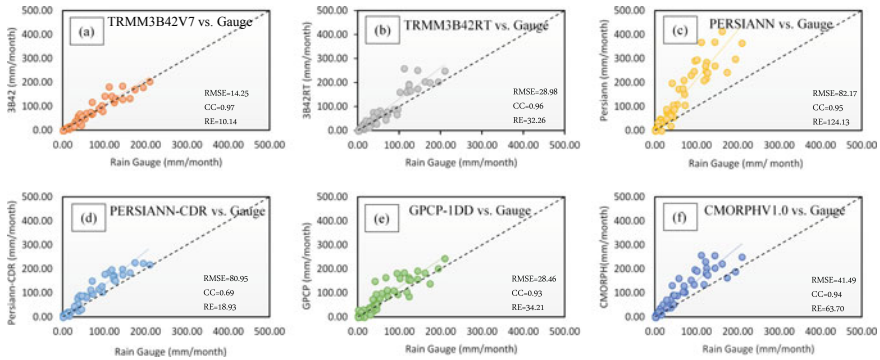
PESPs over the BNB during the period from 2001–2007. Most PESPs (except PERSIANN) typically displayed harmonious patterns of precipitation, with precipitation events decreasing from south to north. However, high precipitation quantities are concentrated in the southern BNB zone in the elevated mountainous areas, and precipitation obviously depends on the basin’s elevation. The precipitation distribution maps also show increases in precipitation in summer (the wet season), especially in August, but precipitation is seen to decrease in winter (the dry season). In both the seasonal and annual spatial patterns, TRMM 3B42V7 reproduced the spatial distributions well against the gauge-based observations. Conversely, the annual and seasonal precipitation patterns obtained with PERSIANN were very distinct with different precipitation intensity distributions.

Figure 8.4 shows the relative volume contributions and the frequency distributions of monthly rainfall at point-based gauge locations in various rainfall event ranges. The monthly precipitation was classified into four groups: 0, 0–100, 100–200, and >200 mm/month. All six PESPs underestimated no rainfall events at the occurrence frequency, while they overestimated small, heavy, and torrential precipitation occurrences (0–100 and >200 mm/month). In terms of moderate rainfall events, all PESPs overestimated their frequencies. The TRMM 3B42V7 estimations were close to the rainfall gauge data for the volume contribution distribution; however, there were some differences compared with the observed gauge-based data. The different performances of volume contributions among PESPs significantly influenced the following hydrological simulations, as most hydrological processes in distributed hydrological models are sensitive to the total precipitation amount and to the distribution of rainfall intensity (Sun et al. 2016). Overall, TRMM 3B42V7 had a greater agreement than the other products when comparing both occurrence frequency and relative volume contribution rate data for moderate



**Fig. 8.4** The occurrence frequencies (bars) of each monthly PESP estimate and their relative volume contributions (lines) to the total rainfall for the 2001–2007 period





**Fig. 8.5** Scatterplots showing monthly precipitation between in situ rainfall observations and PESPs in the BNB during 2001–2007

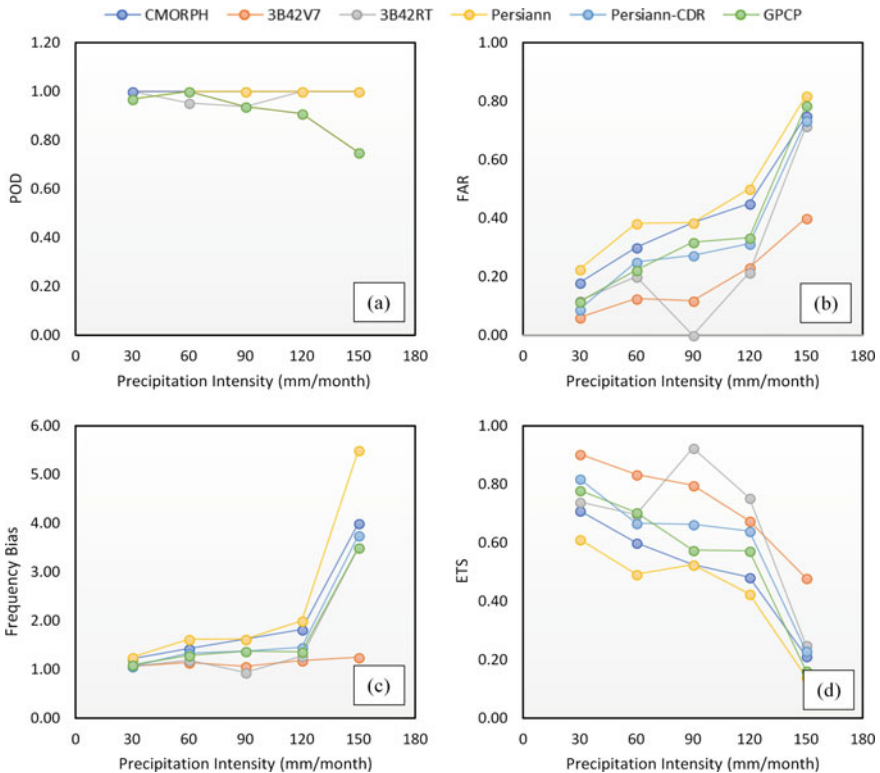
and extreme rainfall events with rain gauge-based data. TRMM 3B42RT, however, had better agreement with the gauge-based data for no rainfall events and small rainfall events.

Figure 8.5 shows the average monthly precipitation scatterplots of six PESPs against in situ rainfall observations and provides further insight into the characteristics of the variations between the six studied PESPs (TRMM 3B42V7, TRMM 3B42RT, GPCP-1DD, CMORPH-V1.0, PERSIANN, and PERSIANN-CDR) and the in situ rainfall observations during the period from 2001 to 2007 over the BNB. In addition, the statistical indicators of the monthly scale estimations of six PESPs are briefly described in Table 8.3. Good agreement can be observed for all PESPs compared with the gauging measurements except PERSIANN. Among these PESPs, TRMM 3B42V7 exhibited the best correspondence against the rain gauge observation data, which is reflected in its CC value of 0.97, the highest among all products, and its RMSE of 14.25 mm/month and RE of 10.14%, the smallest among all products (Fig. 8.5a). Additionally, TRMM 3B42RT and GPCP-1DD showed good performance against the rain gauge observations, with CC values of 0.96 and 0.93 and RMSE values of 28.98 mm/month and 28.46 mm/month, respectively (Fig. 8.5b, e). In contrast, PERSIANN missed the monthly variance for the target basin and presented the poorest values: an RMSE of 82.17 mm/month and an RE of 124.13% (Fig. 8.5c).

**Table 8.3** Statistics of in situ rainfall measurements and PESPs at the monthly timestep

	TRMM 3B42V7	TRMM 3B42RT	CMORPH-V1.0	GPCP-1DD	PERSIANN	PERSIANN-CDR
CC	0.97	0.96	0.94	0.93	0.95	0.69
RMSE	14.25	28.98	41.49	28.46	82.17	80.95
RE (%)	10.14	32.26	63.70	34.21	124.13	18.93

For the categorical statistics, the overall accuracy of the precipitation products (based on POD, FBI, FAR, and ETS) decreased as the rainfall threshold rose, indicating that the studied PESP are less skilled at estimating the exact magnitudes of intense precipitation events. Figure 8.6 illustrates the precipitation detection analysis events over the BNB at several precipitation thresholds, 30 mm/month, 60 mm/month, 90 mm/month, 120 mm/month, and 150 mm/month, using categorical statistics (POD, FBI, FAR, and ETS). All PESP showed POD scores greater than 0.9 (except GPCP-1DD) (Fig. 8.6a). However, for FAR, TRMM 3B42V7 showed the lowest value across all precipitation ranges; meanwhile, the best score was observed for TRMM 3B42RT for the threshold of 90 mm/month (Fig. 8.6b). In general, TRMM 3B42V7 had the best FAR, ETS and FBI values, indicating that it exhibited the best performance across all precipitation ranges. At the same time, PERSIANN demonstrated the weakest performance for the categorical statistics.



**Fig. 8.6** a POD, b FAR, c FBI, and d ETS values of the six monthly PESP against rain gauge observations at 30 mm/month, 60 mm/month, 90 mm/month, 120 mm/month and 150 mm/month threshold values over the BNB during 2001–2007

### 8.3.2 Comparison and Hydrologic Evaluations of Streamflow

According to Bitew and Gebremichael (2011), there are two advantages to evaluating PESP based on their predictive flow rate performances in a hydrologic modeling framework. One of them is that PESP are evaluated as a driving input variable in a hydrological model concerning a specific application. In the prior section, all PESP were compared against the gauge-based observations; the subsequent phase was designed to evaluate how these PESP influenced streamflow simulations by driving the Hydro-BEAM model over the BNB. The streamflow simulation using the Hydro-BEAM Model was calibrated by comparing the measured discharge to examine the efficacy of the six studied PESP over BNB during the calibration period. The Hydro-BEAM model was then forced by CMORPH-V1.0-RAW, TRMM 3B42V7, TRMM 3B42RT, PERSIANN, PERSIANN-CDR, and GPCP-1DD as inputs for seven years (2001–2007) by maximizing the NSE value and the previous model parameter values. Figure 8.7 shows the monthly measured discharge hydrograph compared with the simulated hydrographs in the calibration (from 2001 to 2003) and validation (2004–2007) periods at Khartoum Station. Overall, the simulated hydrographs are noted to be in good agreement with the observed hydrograph, but in some cases, the simulated flows are either underestimated or overestimated compared to the high peaks observed. However, the simulated streamflows presented the relatively low performances of some PESP in the validation period.

The exceedance probability between the monthly measured and simulated discharges is dependent on the rain gauge observations, and the six studied PESP, used as rainfall drivers in the BNB for the interval 2001–2007, are shown in Fig. 8.8. In the calibration period, the exceedance probability plots indicated underestimations of high streamflows for all PESP and overestimations of low streamflows for all PESP (Fig. 8.8a). On the other hand, in the validation period, all PESP showed underestimations of high streamflows and overestimations of low streamflows (except PERSIANN and CMORPH-V1.0) (Fig. 8.8b). As the statistical measures briefly described in Table 8.4, the three statistical indices used to measure the efficiency of the model showed perfect agreement between the observed and simulated hydrographs during the calibration period and reasonable simulations conducted during the validation period. According to the statistical metrics that reflect the model performances, the Hydro-BEAM model can capture the timing, occurrence, and magnitude of the rainfall events shown in the monthly observed hydrograph quite well. Although these metric indices were reasonable for the validation period, they were not as good as those obtained during the calibration period, which indicates better agreement during this period.

The simulation forced by the TRMM 3B42V7 product had the best NSE (0.88 and 0.85), Bias (10.35% and  $-2.87\%$ ), and  $R^2$  (0.94 and 0.92) values during the calibration and validation periods, respectively. The predicted streamflow results were in good correspondence with the observed streamflow data (see Fig. 8.7a,

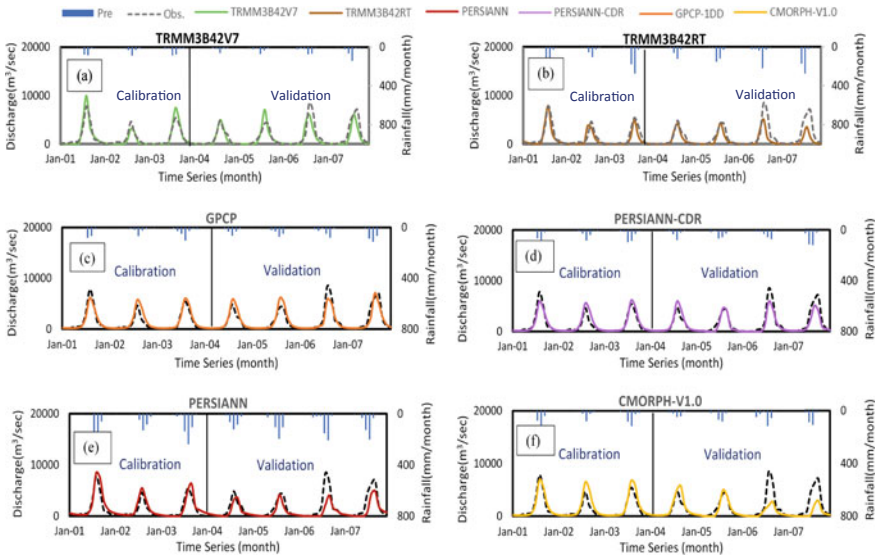


**Fig. 8.7** Hydrographs of Hydro-BEAM-simulated and measured monthly discharges for the calibration (2001–2003) and validation (2004–2007) periods (separated by the vertical line)

Table 8.4). The GPCP-1DD- and TRMM 3B42RT-forced simulations also showed good agreements with the observed streamflow throughout the calibration period, with NSE values of 0.87 and 0.87, Bias values of 12.23 and 17.31%, and  $R^2$  values of 0.94 and 0.95, respectively. These products exhibit slightly less performances in the validation period, with NSE values of 0.85 and 0.84,  $R^2$  values of 0.92 and 0.92, and Bias values of 1.15% and 2.95%, respectively (Fig. 8.7b, c; Table 8.4). Conversely, the PERSIANN and CMORPH-V1.0 simulations showed fair performances, with NSE values of 0.59 and 0.42, Bias values of -38.01% and -31.86%,

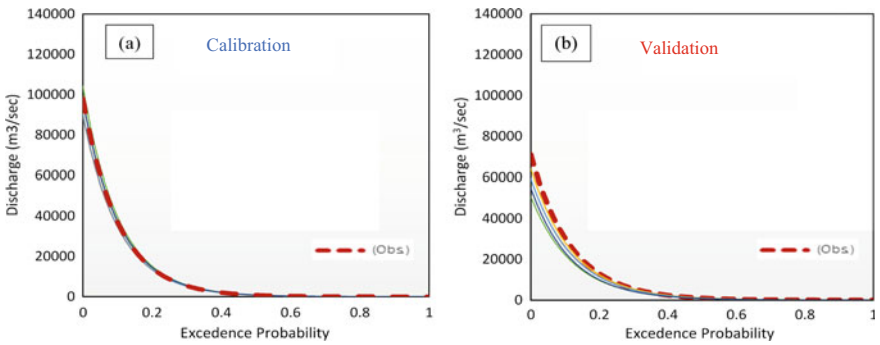


**Fig. 8.8** Exceedance probabilities of monthly discharge in the **a** calibration period and **b** validation period

**Table 8.4** Statistical monthly summary measures of PESP inputs and corresponding streamflows during the calibration and validation periods

Datasets	Calibration			Validation		
	NSE	$R^2$	Bias (%)	NSE	$R^2$	Bias (%)
TRMM 3B42V7	0.88	0.94	10.35	0.85	0.92	- 2.87
GPCP-1DD	0.87	0.94	12.23	0.85	0.92	1.15
TRMM 3B42RT	0.87	0.95	17.31	0.84	0.92	2.95
PERSIANN-CDR	0.86	0.94	11.30	0.83	0.93	- 17.28
PERSIANN	0.79	0.94	25.79	0.59	0.84	- 38.01
CMORPH-V1.0	0.78	0.94	27.67	0.42	0.68	- 31.86

and  $R^2$  values of 0.84 and 0.68 in the validation period, respectively (Fig. 8.7e, f; Table 8.4). Generally, the TRMM 3B42V7 simulations gave the best performance with the Hydro-BEAM model among all PESPs over the BNB during the simulation period (2001–2007). The PERSIANN and CMORPH-V1.0 are not recommended for direct use, as they showed lower abilities to simulate streamflow over the target basin. Therefore, bias removal in PESPs is key to enhancing the truthfulness of hydrologic simulations (Bitew and Gebremichael 2011).

## 8.4 Conclusions

PESPs are recognized as viable sources of precipitation data for use in various hydrologic models for water resource management worldwide and for regional and global hydrologic applications, particularly in data-sparse regions with poor or nonexistent rain gauge measurements. In the current study, a comprehensive analysis was performed to better understand the reliability, precision, and applicability of six PESP (TRMM 3B42V7, TRMM 3B42RT, PERSIANN, PERSIANN-CDR, CMORPH-V1.0, and GPGP-1DD) against rain gauge measurements over the BNB during 2001–2007. Precipitation distribution maps over the BNB were presented based on the six PESP, which are obviously dependent on the basin's elevation. It can also be noticed that the precipitation variation increased in summer (the wet season), especially in August, but decreased in winter (the dry season). Statistical analysis indicated that most PESP could capture the occurrence, timing, and magnitude of precipitation events. In particular, TRMM 3B42V7 typically presented a stronger ability to detect precipitation events than did the other products and correlated well with rain gauge measurements. Moreover, the best FAR, ETS, and FBI were obtained for TRMM 3B42V7 across all precipitation thresholds. Conversely, PERSIANN mostly displayed the lowest estimations of the entire precipitation (Bias), with a high RMSE. Additionally, PERSIANN showed the worst results for the categorical statistics, although it had a better POD score than did the other products.

For streamflow modeling, the predictive capacity of each PESP was examined using the Hydro-BEAM model after a calibration with the observed measurements was conducted. In general, all products achieved reasonable NSE and  $R^2$  values for their estimations of streamflow series at the monthly timestep during the calibration and validation periods (except CMORPH-V1.0 in the validation period). The streamflow simulation results based on TRMM 3B42V7 provided the best correspondence with the measured discharge series compared with the other PESPs. Moreover, the results revealed that TRMM 3B42V7 may be another potential source of data for the area characterized by sparse rainfall gauges in the BNB. In contrast, the PERSIANN and CMORPH-V1.0 products demonstrated lower potentials for utility in hydrologic applications over the BNB.

In summary, the six studied PESPs showed considerable potential for hydrological applications and research. Among the six PESPs, TRMM 3B42V7 exhibited the best performance when compared with observed, gauge-based data in terms of all analyzed criteria over the BNB region, followed by GPCP-1DD and TRMM 3B42RT. By contrast, CMORPH-V1.0 showed fair agreement compared to the other products. The evaluation of the six PESP-based simulations performed for the BNB may not be valid for other areas characterized by different hydroclimatic regimes. In general, this research hopefully offers a good understanding of the utility and uncertainties of various PESPs in streamflow simulations and forecasts and water resource planning and management with satellite-based rainfall data, particularly in data-scarce catchments. Future studies are required to disclose PESP applications under the conditions of climate change, different initial conditions, and among various basins, especially those in data-sparse and ungauged regions.

## References

- Abd-El Moneim H, Soliman MR, Moghazy HM (2017) Numerical simulation of Blue Nile Basin using distributed hydrological model. In: 11th international conference on the role of engineering towards a better environment (RETBE' 17)
- Abd-El Moneim H, Soliman MR, Moghazy HM (2019) Hydrologic evaluation of TRMM multi-satellite precipitation analysis products over Blue Nile Basin. In: 2nd international conference of chemical, energy and environmental engineering (ICCEE2019), pp 33–44
- Abdel-Fattah M (2017) A hydrological and geomorphometric approach to understanding the generation of wadi flash floods. A Hydrological and Geomorphometric Approach to. <https://doi.org/10.3390/w9070553>
- Abdel-Fattah M, Kantoush S, Sumi T (2015) Integrated management of flash flood in wadi system of Egypt: disaster prevention and water harvesting. *Annu Disas Prev Res Inst, Kyoto Univ* 58:485–496
- Abdelmoneim H, Soliman MR, Moghazy HM (2020) Evaluation of TRMM 3B42V7 and CHIRPS satellite precipitation products as an input for hydrological model over eastern Nile Basin. *Earth Syst Environ* 4:685–698. <https://doi.org/10.1007/s41748-020-00185-3>
- Alazzy AA, Lü H, Chen R et al (2017) Evaluation of satellite precipitation products and their potential influence on hydrological modeling over the Ganzi River Basin of the Tibetan Plateau. *Adv Meteorol* 2017. <https://doi.org/10.1155/2017/3695285>

- Ali AF, Xiao C, Anjum MN et al (2017) Evaluation and comparison of TRMM multi-satellite precipitation products with reference to rain gauge observations in Hunza River basin, Karakoram Range, northern Pakistan. *Sustain* 9. <https://doi.org/10.3390/su9111954>
- Ashouri H, Hsu KL, Sorooshian S et al (2015) PERSIANN-CDR: daily precipitation climate data record from multisatellite observations for hydrological and climate studies. *Bull Am Meteorol Soc* 96:69–83. <https://doi.org/10.1175/BAMS-D-13-00068.1>
- Awulachew SB, McCartney M, Steenhuis TS, Ahmed AA (2008) A review of hydrology, sediment and water resource use in the Blue Nile Basin (IWMI Working Paper 131)
- Behrangi A, Khakbaz B, Jaw TC et al (2011) Hydrologic evaluation of satellite precipitation products over a mid-size basin. *J Hydrol* 397:225–237. <https://doi.org/10.1016/j.jhydrol.2010.11.043>
- Bitew MM, Gebremichael M (2011) Evaluation of satellite rainfall products through hydrologic simulation in a fully distributed hydrologic model. *Water Resour Res* 47:1–11. <https://doi.org/10.1029/2010WR009917>
- Bitew MM, Gebremichael M, Ghebremichael LT, Bayissa YA (2012) Evaluation of high-resolution satellite rainfall products through streamflow simulation in a hydrological modeling of a small mountainous watershed in Ethiopia. *J Hydrometeorol* 13:338–350. <https://doi.org/10.1175/2011JHM1292.1>
- Fenta AA, Yasuda H, Shimizu K et al (2018) Evaluation of satellite rainfall estimates over the Lake Tana basin at the source region of the Blue Nile River. *Atmos Res* 212:43–53. <https://doi.org/10.1016/j.atmosres.2018.05.009>
- Gebere SB, Alamirew T, Merkel BJ, Melesse AM (2015) Performance of high resolution satellite rainfall products over data scarce parts of eastern ethiopia. *Remote Sens* 7:11639–11663. <https://doi.org/10.3390/rs70911639>
- Gebrehiwot SG, Istedt U, Gärdenas AI, Bishop K (2011) Hydrological characterization of watersheds in the Blue Nile Basin, Ethiopia. *Hydrol Earth Syst Sci* 15:11–20. <https://doi.org/10.5194/hess-15-11-2011>
- Gebremicael TG, Mohamed YA, Van Der Zaag P, Amdom G (2017) Comparison and validation of eight satellite rainfall products over the rugged topography of Tekeze-Atbara Basin at different spatial and temporal scales. *Hydrol Earth Syst Sci Discuss* 1–31. <https://doi.org/10.5194/hess-2017-504>
- Habib E, Haile AT, Tian Y, Joyce RJ (2012) Evaluation of the high-resolution CMORPH satellite rainfall product using dense rain gauge observations and radar-based estimates. *J Hydrometeorol* 13:1784–1798. <https://doi.org/10.1175/JHM-D-12-017.1>
- Hirpa FA, Gebremichael M, Hopson T (2010) Evaluation of high-resolution satellite precipitation products over very complex terrain in Ethiopia. *J Appl Meteorol Climatol* 49:1044–1051. <https://doi.org/10.1175/2009JAMC2298.1>
- Hsu K, Gao X, Sorooshian S, Gupta HV (1997) Precipitation estimation from remotely sensed information using artificial neural networks. *J Appl Meteorol* 36:1176–1190. [https://doi.org/10.1175/1520-0450\(1997\)036%3c1176:PEFRSI%3e2.0.CO;2](https://doi.org/10.1175/1520-0450(1997)036%3c1176:PEFRSI%3e2.0.CO;2)
- Huang Y, Chen S, Cao Q et al (2014) Evaluation of version-7 TRMM multi-satellite precipitation analysis product during the Beijing extreme heavy rainfall event of 21 July 2012. *Water (switzerland)* 6:32–44. <https://doi.org/10.3390/w6010032>
- Huffman GJ, Adler RF, Arkin P et al (1997) The global precipitation climatology project (GPCP) combined precipitation dataset. *Bull Am Meteorol Soc* 78:5–20. [https://doi.org/10.1175/1520-0477\(1997\)078%3c0005:TGPCPG%3e2.0.CO;2](https://doi.org/10.1175/1520-0477(1997)078%3c0005:TGPCPG%3e2.0.CO;2)
- Huffman GJ, Bolvin DT, Nelkin EJ et al (2007) The TRMM multisatellite precipitation analysis (TMPA): quasi-global, multiyear, combined-sensor precipitation estimates at fine scales. *J Hydrometeorol* 8:38–55. <https://doi.org/10.1175/JHM560.1>
- Jiang Q, Li W, Wen J et al (2018) Accuracy evaluation of two high-resolution satellite-based rainfall products: TRMM 3B42V7 and CMORPH in Shanghai. *Water (Switzerland)* 10. <https://doi.org/10.3390/w10010040>
- Jiang S, Ren L, Hong Y et al (2012) Comprehensive evaluation of multi-satellite precipitation products with a dense rain gauge network and optimally merging their simulated hydrological

- flows using the Bayesian model averaging method. *J Hydrol* 452–453:213–225. <https://doi.org/10.1016/j.jhydrol.2012.05.055>
- Joyce RJ, Janowiak JE, Arkin PA, Xie P (2004) CMORPH: a method that produces global precipitation estimates from passive microwave and infrared data at high spatial and temporal resolution. *J Hydrometeorol* 5:487–503. [https://doi.org/10.1175/1525-7541\(2004\)005%3c0487:CAMTPG%3e2.0.CO;2](https://doi.org/10.1175/1525-7541(2004)005%3c0487:CAMTPG%3e2.0.CO;2)
- Joyce RJ, Xie P, Yarosh Y et al (2010) CMORPH: a “Morphing” approach for high resolution precipitation product generation
- Karamouz M, Nazif S, Falahi M (2013) *Hydrology and hydroclimatology\_ principles and applications*. CRC Press, U.S.
- Knapp KR (2008) Scientific data stewardship of international satellite cloud climatology project B1 global geostationary observations. *J Appl Remote Sens* 2:023548. <https://doi.org/10.1117/1.3043461>
- Kojiri T, Tokai A, Kinai Y (1998) Assessment of river basin environment through simulation with water quality and quantity. *Annu Disaster Prev Res Inst Kyoto Univ* 41:119–134
- Kubota T, Hashizume H, Shige S et al (2007) Global precipitation map using satelliteborne microwave radiometers by the GSMaP project: production and validation. In: *IEEE transactions on geoscience and remote sensing abbreviated*. Institute of Electrical and Electronics Engineers Inc, pp 2259–2275
- Kummerow C, Barnes W, Kozu T et al (1998) The tropical rainfall measuring mission (TRMM) sensor package. *J Atmos Ocean Technol* 15:809–817. [https://doi.org/10.1175/1520-0426\(1998\)015%3c0809:TTRMMT%3e2.0.CO;2](https://doi.org/10.1175/1520-0426(1998)015%3c0809:TTRMMT%3e2.0.CO;2)
- Lakew HB, Moges SA, Asfaw DH (2017) Hydrological evaluation of satellite and reanalysis precipitation products in the Upper Blue Nile Basin: a case study of Gilgel Abbay. *Hydrology* 4:39. <https://doi.org/10.3390/hydrology4030039>
- Legates DR, McCabe GJ Jr (1999) Evaluating the use of “Goodness of Fit” measures in hydrologic and hydroclimatic model validation. *Water Resour Res* 35:233–241. <https://doi.org/10.1029/1998WR900018>
- Li Y, Wang W, Lu H et al (2019) Evaluation of three satellite-based precipitation products over the lower Mekong River Basin using rain gauge observations and hydrological modeling. *IEEE J Sel Top Appl Earth Obs Remote Sens* 12:2357–2373. <https://doi.org/10.1109/jstars.2019.2915840>
- MWRI (1998a) Measured discharges of the Nile and /its tributaries every 5 years. Egypt
- MWRI (1998b) Monthly and annual rainfall totals and number of rainy days at stations in and near the Nile Basin for every 5 years. Egypt
- Ragab O, Valeriano OCS (2014) Flood forecasting in Blue Nile Basin using a process-based distributed hydrological model and satellite distributed hydrological model and satellite derived precipitation product. In: *ASEE 2014 Zone I conference, USA*
- Romilly TG, Gebremichael M (2011) Evaluation of satellite rainfall estimates over Ethiopian river basins. *Hydrol Earth Syst Sci* 15:1505–1514. <https://doi.org/10.5194/hess-15-1505-2011>
- Saber M (2010) Hydrological approaches of Wadi system considering flash floods in arid regions. Kyoto University, Japan
- Saber M, Yilmaz K (2016) Bias correction of satellite-based rainfall estimates for modeling flash floods in semi-arid regions: application to Karpuz River, Turkey. *Nat Hazards Earth Syst Sci Discuss* 1–35. <https://doi.org/10.5194/nhess-2016-339>
- Saber M, Yilmaz KK (2018) Evaluation and bias correction of satellite-based rainfall estimates for modelling flash floods over the Mediterranean region: application to Karpuz River Basin, Turkey. *Water (Switzerland)* 10. <https://doi.org/10.3390/w10050657>
- Samy A, Valeriano OCS, Negm A (2015) Variability of hydrological modeling of the Blue Nile. *Int J Environ Chem Ecol Geol Geophys Eng* 9:225–229. <https://doi.org/10.scholar.waset.org/1999.6/10000744>
- Saber M, Hamaguchi T, Kojiri T et al (2013) A physically based distributed hydrological model of wadi system to simulate flash floods in arid regions. *Arab J Geosci* 58:485–496. <https://doi.org/10.1007/s12517-013-1190-0>



- Sapkta M, Hamaguchi T et al. (2010) Hydrological simulations in red river basin using super high resolution GCM outputs with geostatistical process. *Annals of Disas Prev Res Inst, Kyoto Univ.*, No. 53 B
- Schaefer JT (1990) The critical success index as an indicator of warning skill. *Weather Forecast* 5:570–575. [https://doi.org/10.1175/1520-0434\(1990\)005%3c0570:TCSIAA%3e2.0.CO;2](https://doi.org/10.1175/1520-0434(1990)005%3c0570:TCSIAA%3e2.0.CO;2)
- Sorooshian S, Hsu K, Gao X et al (2000) Evaluation of PERSIANN system satellite based estimates of tropical rainfall. *Bull Am Meteorol Soc* 81:2035–2046. [https://doi.org/10.1175/1520-0477\(2000\)081%3c2035:EOPSSE%3e2.3.CO;2](https://doi.org/10.1175/1520-0477(2000)081%3c2035:EOPSSE%3e2.3.CO;2)
- Stisen S, Sandholt I (2010) Evaluation of remote-sensing-based rainfall products through predictive capability in hydrological runoff modelling. *Hydrol Process* 24:879–891. <https://doi.org/10.1002/hyp.7529>
- Sun R, Yuan H, Liu X, Jiang X (2016) Evaluation of the latest satellite-gauge precipitation products and their hydrologic applications over the Huaihe River basin. *J Hydrol* 536:302–319. <https://doi.org/10.1016/j.jhydrol.2016.02.054>
- Tong K, Su F, Yang D, Hao Z (2014) Evaluation of satellite precipitation retrievals and their potential utilities in hydrologic modeling over the Tibetan Plateau. *J Hydrol* 519:423–437. <https://doi.org/10.1016/j.jhydrol.2014.07.044>
- Walters BMO (1990) Transmission losses in arid region. *J Hydraulic Eng* 116:129–138
- Wang S, Liu S, Mo X et al (2015) Evaluation of remotely sensed precipitation and its performance for streamflow simulations in basins of the Southeast Tibetan Plateau. *J Hydrometeorol* 16:2577–2594. <https://doi.org/10.1175/JHM-D-14-0166.1>
- Wilks DS (2006) *Statistical methods in the atmospheric sciences*, 2nd edn
- Xie P, Arkin PA (1995) An Intercomparison of gauge observations and satellite estimates of monthly precipitation. *J Appl Meteorol* 34:1143–1160. [https://doi.org/10.1175/1520-0442\(1996\)009%3c0840:AOGMPU%3e2.0.CO;2](https://doi.org/10.1175/1520-0442(1996)009%3c0840:AOGMPU%3e2.0.CO;2)
- Xue X, Hong Y, Limaye AS et al (2013) Statistical and hydrological evaluation of TRMM-based multi-satellite precipitation analysis over the Wangchu Basin of Bhutan: are the latest satellite precipitation products 3B42V7 ready for use in ungauged basins? *J Hydrol* 499:91–99. <https://doi.org/10.1016/j.jhydrol.2013.06.042>

**Open Access** This chapter is licensed under the terms of the Creative Commons Attribution 4.0 International License (<http://creativecommons.org/licenses/by/4.0/>), which permits use, sharing, adaptation, distribution and reproduction in any medium or format, as long as you give appropriate credit to the original author(s) and the source, provide a link to the Creative Commons license and indicate if changes were made.

The images or other third party material in this chapter are included in the chapter's Creative Commons license, unless indicated otherwise in a credit line to the material. If material is not included in the chapter's Creative Commons license and your intended use is not permitted by statutory regulation or exceeds the permitted use, you will need to obtain permission directly from the copyright holder.

